Science Advances

AAAS

advances.sciencemag.org/cgi/content/full/3/9/e1701558/DC1

Supplementary Materials for

Self-determined shapes and velocities of giant near-zero drag gas cavities

Ivan U. Vakarelski, Evert Klaseboer, Aditya Jetly, Mohammad M. Mansoor, Andres A. Aguirre-Pablo, Derek Y. C. Chan, Sigurdur T. Thoroddsen

Published 8 September 2017, *Sci. Adv.* **3**, e1701558 (2017)
DOI: 10.1126/sciadv.1701558

The PDF file includes:

- section S1. Theory: Achieving near-zero drag at high Reynolds numbers
- section S2. Stable streamlined cavity experiments
- section S3. Solid projectile experiments
- section S4. Determination of the drag coefficients
- fig. S1. The experimental apparatus.
- fig. S2. 3D-printed solid projectiles.
- fig. S3. Comparison of shapes of sphere-in-cavities and solid projectiles.
- fig. S4. Three-piece fitting function for the sphere-in-cavity.
- fig. S5. Velocity versus depth data.
- fig. S6. Dependence of the drag coefficient on the aspect ratio.
- table S1A. Physical parameters of the sphere-in-cavities in 95°C water.
- table S1B. Physical parameters of the sphere-in-cavities in 21°C water.
- table S1C. Physical parameters of the sphere-in-cavities in PP1 liquid.
- Legends for movies S1 to S4
- Reference (*29*)

Other Supplementary Material for this manuscript includes the following:
(available at advances.sciencemag.org/cgi/content/full/3/9/e1701558/DC1)

- movie S1 (.mov format). Free fall of sphere-in-cavity for 10-mm Leidenfrost steel sphere in PP1.
- movie S2 (.mov format). Impact and cavity formation by 20-mm steel sphere in 21° and 95°C water.

- movie S3 (.mov format). Close-up of sphere-in-cavity for 20-mm steel sphere in 21° and 95°C water.
- movie S4 (.mov format). Comparison of solid projectiles and sphere-in-cavity free fall.

section S1. Theory: Achieving near-zero drag at high Reynolds numbers

Here we develop the theoretical analysis for the required properties of an object that can move with nearly zero drag and thereby almost achieve perpetual motion.

The flow associated with an object moving at velocity U, in a Newtonian fluid of density ρ and shear viscosity μ, is characterized by the Reynolds number, $\mathrm{Re} \equiv \rho DU/\mu$, where D is the characteristic length scale of the object, e.g. $D = 2R$ for a sphere of radius, R. The velocity field, $u(\mathbf{r})$ in the fluid can be found by solving the Navier-Stokes momentum equation (*5*)

$$\rho \frac{\partial \mathbf{u}}{\partial t} + \rho\, \mathbf{u} \cdot \nabla \mathbf{u} \; - \mu \nabla^2 \mathbf{u} \; = -\nabla P + \rho \mathbf{g} \tag{S1}$$

where we have included a body force term due to gravity, $\mathbf{g}$.

For an irrotational flow: $\nabla \times \mathbf{u} = \mathbf{0}$ with the incompressibility condition: $\nabla \cdot \mathbf{u} = 0$, the velocity potential: $\mathbf{u} = \nabla \phi$ satisfies the Laplace equation: $\nabla^2 \phi = 0$.

At high velocities, Re >> 1, viscous effects can be neglected for flow far from the object where the pressure and the velocity will be related by the Bernoulli equation that can be obtained by integrating (S1)

$$P + \rho \frac{\partial \phi}{\partial t} + \tfrac{1}{2} \rho\, u^2 - \rho g z = P + \rho \frac{\partial \phi}{\partial t} + \tfrac{1}{2} \rho\, |\nabla \phi|^2 - \rho g z = \text{constant} \tag{S2}$$

where gravity is in the z-direction: $\mathbf{g} = g\, \mathbf{k}$. However, depending on the boundary condition on the surface of the moving object, viscosity effects may not be negligible in determining the flow field near the surface of the object because of boundary layer effects (*5*).

For a steadily translating solid sphere of radius R, for which the fluid layer adjacent to its surface moves at the same speed as the sphere, this "no-slip" boundary condition creates a boundary layer in which viscosity effects cannot be omitted. The transition of this boundary layer to turbulence is responsible for the so-called drag crisis, characterized by the sudden decrease of the drag coefficient at a critical Reynolds numbers. For a sphere moving at constant velocity, U under the influence of an applied force, F the drag coefficient, $C_D(\mathrm{Re})$, a function of Re, is defined by:

$$F \equiv \left(\frac{1}{2}\rho\, U^2\right)(\pi R^2)\, C_D(\mathrm{Re}) \tag{S3}$$

For Reynolds numbers between 10^3 to 10^5, the drag coefficient is nearly constant, $C_D(\mathrm{Re}) \sim 0.4$, but at the critical $\mathrm{Re} \geq 3 \times 10^5$, C_D drops rapidly to ~ 0.1, marking the onset of the drag crisis as the boundary layer transitions to turbulence (*29*).

In contrast, for the corresponding steady state problem of a hypothetical sphere where the liquid is free to move tangentially along the surface, this "free-slip" boundary condition can be satisfied without consideration of viscous effects. The resulting flow field is then given by the potential flow solution. In this case, the pressure, P on the surface of such a "free-slip" sphere of radius R travelling at constant velocity U, in the z-direction in an ideal fluid of density ρ, has the form (assuming gravity, $g = 0$) (*1*)

$$P(r = R, \theta) - P_0 = \frac{1}{2}\rho\, U^2 \left[1 - \frac{9}{4}\sin^2\theta\right] \tag{S4}$$

Therefore, the pressure, relative to the reference value, P_0 where the velocity field: $\mathbf{u}_0 = -U\,\mathbf{k}$ is constant, takes on the maximum value of $\left(\frac{1}{2}\rho\, U^2\right)$, known as the stagnation pressure, at the front and rear stagnation points corresponding to $\theta = 0$ and π, respectively. The negative minimum value: $\left(-\frac{5}{8}\rho\, U^2\right)$ that occurs at the equator ($\theta = \pi/2$), indicates a suction and is the consequence of the steady state Bernoulli equation (with $g = 0$ and $\partial/\partial t = 0$)

$$P = \left\{P_0 + \frac{1}{2}\rho\, U^2\right\} - \frac{1}{2}\rho\, u^2 \tag{S5}$$

where the term in $\{\ldots\}$ is a constant such that the pressure is P_0 where the velocity is U. Equation (S5) implies that an increase in the magnitude of the velocity, for example, for u near the equator, $\theta \sim \pi/2$ of a sphere, will because of fluid incompressibility, result in a decrease in the pressure, P. This is the well-known Bernoulli effect.

Since the pressure variation on the surface of this translating "free-slip" sphere in (S4) has fore-aft symmetry, the net force experienced by the sphere obtained from the integral of the pressure over the sphere surface is zero. This is the d'Alembert Paradox, as a "free-slip" sphere can travel at any velocity, U and experiences no resistance or drag force if we assume the fluid is inviscid.

However, the flow field generated by the motion of such a "free-slip" sphere in a viscous fluid does result in a non-zero drag. For large Re, the drag has been estimated by using the inviscid potential flow velocity field to calculate the dissipation and hence the drag coefficient (*3,4*)

$$C_D(\mathrm{Re}) \cong \left(\frac{48}{\mathrm{Re}}\right)\left\{1 - \frac{2.2}{\mathrm{Re}^{1/2}} + \cdots\right\}, \qquad \mathrm{Re} \to \infty \tag{S6}$$

that becomes negligibly small as the Reynolds number increases.

Herein we have constructed a body with minimum drag resistance under similar conditions since the "free-slip" boundary can be satisfied as closely as possible at the "stress-free" liquid-gas interface of the gas cavity that completely encloses a solid sphere in a sphere-in-cavity structure. However, it is not possible to maintain a spherical interface at large Reynolds number, as the sphere-in-cavity will adjust the shape of the gas boundary to minimize drag in accordance to the principle of minimal dissipation. As the sphere-in-cavity travels in the direction of gravity the steady state Bernoulli equation, from (S2) will now have the form

$$P = \left\{P_0 + \tfrac{1}{2}\rho\, U^2 - \rho g z_0\right\} - \tfrac{1}{2}\rho\, u^2 + \rho g z \tag{S7}$$

where the term in $\{\ldots\}$ is a constant such that at z_0, the pressure is P_0 and the velocity is U.

The typical physical parameters of our tear drop shape sphere-in-cavity have cross-sectional diameter, D ~ 25 mm, length, L ~ 100 mm and velocity, U ~ 2 m/s. The corresponding magnitudes of the dynamic pressure, $\frac{1}{2}\rho\, U^2 \sim 2 \times 10^3$ Pa and the gravitational pressure $\rho g L_c \sim 10^3$ Pa are therefore comparable. The contribution from the air-water interfacial tension, σ = 72 mN/m, to a Laplace pressure, $2\sigma/D \sim 6$ Pa, is sufficiently small to be neglected to a good approximation. This suggests that the dominant effects are the dynamic and the gravitational pressure, and therefore the foregoing discussion of potential flow in a gravitational field captures the key physical attributes of the experiments.

The shape of the sphere-in-cavity is axisymmetric, therefore we can extract its shape from images of the high speed video to construct the surface of the sphere-in-cavity and use that to obtain the velocity potential ϕ and hence obtain the velocity, $\mathbf{u} = \nabla\phi$ by solving the Laplace equation for ϕ and using an axisymmetric boundary integral method (*28*).

The pressure inside the air-cavity should be constant, due to the much lower density of the gas. If we now consider this solution on the gas surface of the sphere-in-cavity where the pressure *P* must also be constant, then from the Bernoulli equation (S7) we expect that the variation of the dynamic pressure, $\frac{1}{2}\rho\, u^2$ will balance the gravitational pressure, $\rho g z$ within the liquid next to the free surface. However, around the nose of the sphere-in-cavity, the shape must conform to that of the solid sphere and therefore we expect the pressure variation to follow (S4) in this part of the sphere-in-cavity.

The results in the main paper show that the experimental results do indeed agree with these expectations. However, although the sphere-in-cavity has a near zero drag like the hypothetical "free-slip" sphere, a significant feature is that its velocity can no longer take on any value as in the case of the sphere. The self-determined shape of the sphere-in-cavity produces a dynamic pressure profile that balances the gravitational pressure in the Bernoulli equation (S7) and this then determines the velocity of the sphere-in-cavity. Therefore, as the sphere-in-cavity adopts the self-determined shape to minimize dissipation and drag, this process also determines the velocity at which this can occur.

Finally, regarding the shape of the cavity tail: We expect the free-surface streamlines to merge at the back without a stagnation point. However, at the sharp cusp, surface tension will break up the shape resulting in a small irregular stagnating gas/liquid region which has the same pressure as the gas cavity. The tip of the cavity is indeed observed to be rather irregular in the experiments, not like the sharp tip in the numerical simulations.

section S2. Stable streamlined cavity experiments

In these experiments we use high-speed video recording to measure the shape and the fall velocity of a solid sphere enveloped with a stable streamline gas cavity (sphere-in-cavity) falling through water or fluorocarbon, PP1 liquid. The sphere-in-cavity forms after a solid sphere is released in the air above a deep tank of liquid and impact and crosses the air-liquid interface and

thereby entrains an air envelop as it continues into the liquid. Three types of experiments were conducted: (i) cavities formed following the impact of heated steel or tungsten carbide spheres (heated to an initial temperature, T_S = 400 ºC) onto 95 ºC water; (ii) cavities formed by the impact of superhydrophobic steel spheres onto room temperature, 21 ºC water and (iii) cavities formed following the impact of heated steel or tungsten carbide spheres (at temperature, T_S = 230 ºC) onto the perfluorocarbon liquid, PP1. The experimental protocol is similar to that used in our recent study on streamlined and helical wake formation by the impact of Leidenfrost spheres on perfluorocarbon liquid, PP1 (*20*). Specific details relevant to the present experiments are given below.

A schematic of the experimental setup is given in fig. S1. The custom manufactured liquid tank and heater device was produced by ChangTong Science and Technology (TianJin) Co. LTD, China. The liquid tank is 2 m tall with cross-section of dimensions 20 × 20 cm. Electric heaters installed in a chamber beneath the tank base allow the water to be heated up to 100 ºC. The front and the back sides of the tank are double-glazed glass windows. The same device was used in our earlier work on Leidenfrost spheres undergoing free fall in water (*14*), which contains further device operational details.

The spheres used were polished grinding balls (FRITSCH GmbH) of stainless steel (ρ_s = 7.7 g/cm^3, $D_S = 2R_S$ = 10, 15, 20, 25 mm) or tungsten carbide (ρ_s = 14.9 g/cm^3, $D_S = 2R_S$ = 10, 15, 20 mm). The average surface roughness specified by the manufacturer is less than 0.06 μm. The spheres were rinsed with ethanol and water and dried before use.

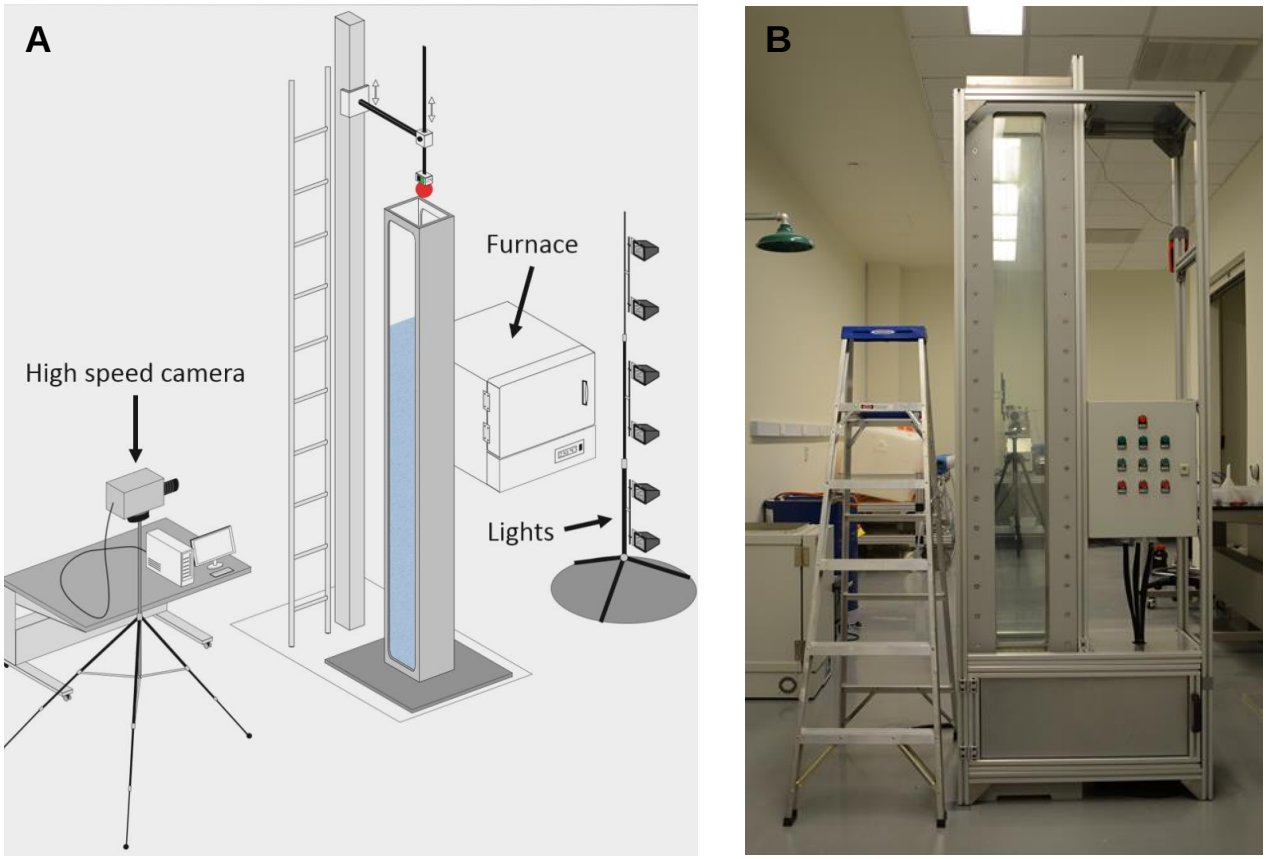

fig. S1. The experimental apparatus. (**A**) Schematic of the experimental setup showing the liquid tank and camera. (**B**) Photograph of the liquid vessel and heater device.

In the 95 ºC water experiments, we used unmodified hydrophilic surface steel or tungsten carbide spheres that were heated to 400 ºC in a high temperature furnace before the release into the tank. The initial sphere temperature, T_S = 400 ºC was sufficiently high above the static sphere Leidenfrost temperature, T_L of about 260 ºC under such conditions (*14*) to maintain a non-wetting Leidenfrost state on the sphere surface until it reached the bottom of the tank.

Steel spheres with superhydrophobic surfaces were produced by the application of a coating of a commercially available car mirror water-repellent agent: Glaco Mirror Coat “Zero”, Soft 99 Co.

(http://www.soft99.co.jp/en/). The liquid coating is an alcohol-based suspension of silica nanoparticles functionalized by an organic hydrophobizing agent. A detailed description of the coating deposition procedure and characterization of the superhydrophobic coating properties has been given earlier (*25*). The coating on the spheres resulted in excellent superhydrophobic surface properties with a water contact angle of more than 160°.

The detailed dynamics of the formation of the gas cavity around the impacting sphere into water follow a similar pattern as in the case of Leidenfrost sphere impacting a perfluorocarbon liquid, PP1 (Flutec, F2 Chemicals Ltd, UK) introduced in our recent study (*20*). This earlier work included a detailed investigation of the physical mechanisms underlying the formation of three types of cavity wakes: unstable wake formed at lower impact velocities, stable-streamlined cavity wake formed at intermediate impact velocities, and helical wake formed at higher impact velocities. In the present study our focus is to determine the drag coefficient of the sphere enveloped by a stable streamlined gas cavity – sphere-in-cavity. Accordingly, we have not followed the same detailed analysis of the physical processes leading to cavity formation or extensive mapping of the wake type dependence on the sphere release conditions as we have done in the Leidenfrost sphere impact on perfluorocarbon liquid study (*20*). Instead we have only adjusted the sphere release height, h_r above the fluid interface to achieve a steady streamlined cavity that enveloped the sphere. The optimum h_r values for each type of sphere used are given in Table 1 together with the densities and viscosities of the liquids.

section S3. Solid projectile experiments

In these experiments, we use high-speed video recording to measure the terminal velocity of streamlined solid projectiles free falling in water and compare their drag coefficients with the drag coefficients of the sphere-in-cavities.

The 3D-printed solid projectiles were designed using Solidworks (Dassault Systemes S.A.) and then printed using a Create NS (Leapfrog) desktop 3D-printer. Leapfrog MAXX Essentials ABS

filament was the printing material as it was strong and durable and allowed the use of sandpaper to give the projectile surface a smooth finish.

The axisymmetric shape of the projectile is specified by an elliptical front part and a parabolic rear part as shown in fig. S2. Technically it was easiest to print projectiles with dimensions that match approximately that of the 20 mm steel or tungsten carbide spheres cavities. Each projectile is printed as two separate parts: the front (elliptical) and rear (parabolic) part assembled together by a screw thread to form a void in which small metallic ballast spheres can be fitted to adjust the projectile weight as shown in fig. S2. In figure S3 we compare the Solidworks drawings of the projectiles with pictures of the cavity for the case of 20 mm steel and 20 mm tungsten carbide sphere.

Stabilizer fins were added at the rear of the projectile to ensure rectilinear fall inside the tank. To estimate the contribution of the stabilizer to the projectiles drag coefficient we compared the terminal velocity of the same body projectiles but different size of the stabilizers, from 20 × 15 mm to 40 × 30 mm. This way it was estimated that the standard stabilizers size (30 × 20 mm fig. S3) we used accounted for less than 10 % of overall projectile drag in our experiments.

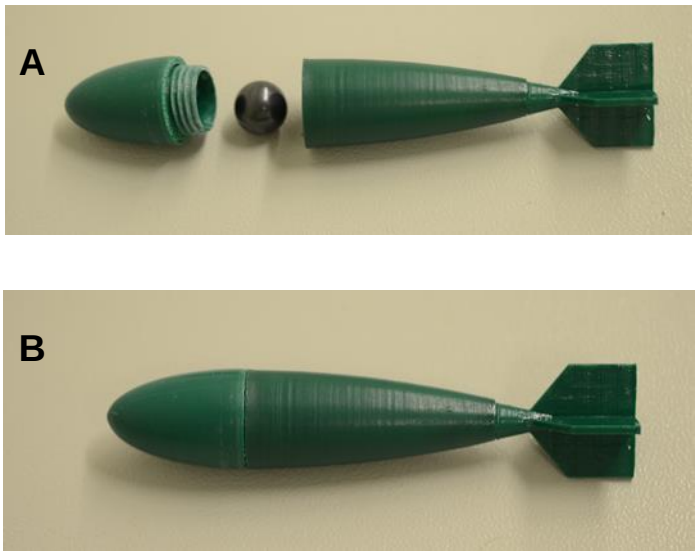

fig. S2. 3D-printed solid projectiles. Photograph of (**A**) the disassembled front and rear part of the projectile with a ballast sphere to be fitted inside and (**B**) the assembled projectile. The axisymmetric shape of the projectile of length, L_P is specified by an elliptical front portion defined by: $y = \pm\left(\frac{D_P}{2L_F}\right)\sqrt{L_F^2 - x^2}, 0 < x < L_F$ and a parabolic rear portion: $y = \pm\left(\frac{D_P}{2}\right)[1 - (x/L_R)^2],\ -L_F < x < 0$. The two forms join at the widest part with thickness, D_P.

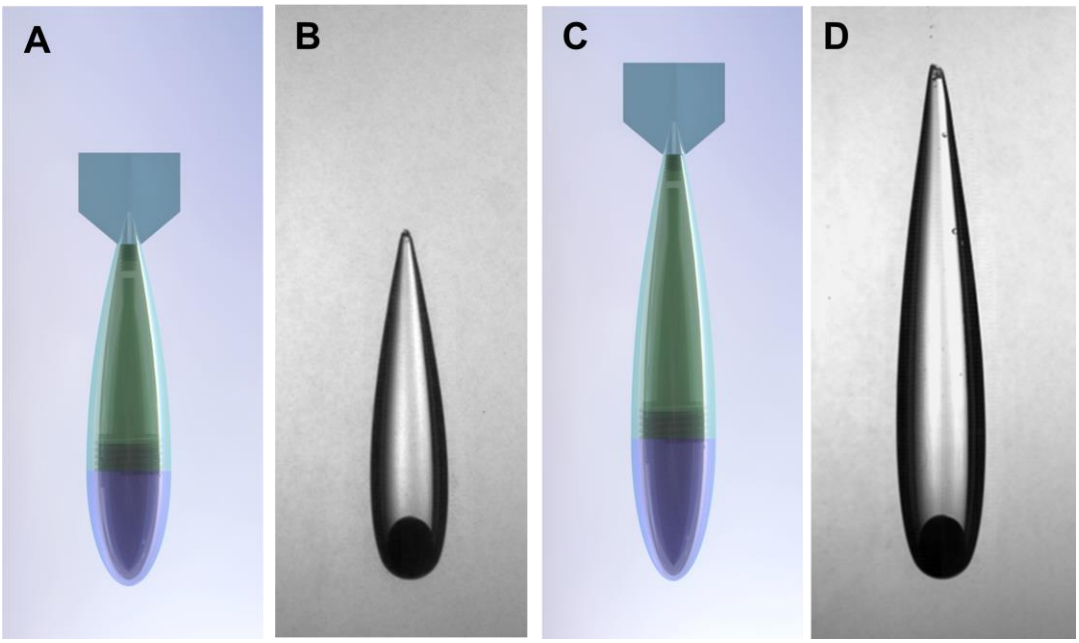

fig. S3. Comparison of shapes of sphere-in-cavities and solid projectiles. Shapes of sphere-in-cavity formed by the impact of Leidenfrost spheres, T_S = 400 ºC onto 95 ºC water: (A, B) 20 mm steel sphere with aspect ratios of the sphere-in-cavity and projectile, $L/D \approx L_P/D_P = 4.5$; (C, D) 20 mm tungsten carbide sphere with sphere-in-cavity aspect ratios, $L/D \approx L_P/D_P = 5.5$. The images of the solid projectiles images were generated by SolidWork.

For the set of experiments shown in Fig. 3 of the manuscript, the dimensions of the projectile are: D_P = 25 mm, L_P = 112 mm and the relative length of the elliptical front section is L_F/L_P = 0.30. For this projectile L_P/D_P = 4.5, which closely matches the L/D ratio for the steel spheres cavities in water (Table 1). For the set of experiments shown in fig. S6 of the manuscript the D_P = 25 mm is fixed, and the L_P is varied to give L_P/D_P = 2.0; 3.0; 3.5; 4.5; 5.5; 7.0, with and the relative length of the elliptical front section fixed at L_F/L_P = 0.30.

section S4. Determination of the drag coefficients

When characterizing the drag on streamlined bodies of revolution, different choices for the characteristic length scale have been used to define the Reynolds number, Re and drag coefficient, C_D. Here we use the maximum cavity diameter, $D = 2R$, so that, $\mathrm{Re} = \rho DU/\mu$ and the cavity front cross-sectional area is used to define the drag coefficient, so that $C_D = F_D/[(\pi R^2)(\rho U^2/2)]$.

The drag coefficient C_D of the streamlined shape cavity was calculated using the following expression that balances the drag force against gravity and buoyancy forces on the sphere-in-cavity falling at terminal velocity U

$$C_D = \frac{2g(m_s - \rho V_c)}{\rho\pi\ R^2\ U^2} \tag{S8}$$

where ρ is the liquid density, m_S the sphere mass, g the gravity constant, and V_C the cavity volume (which includes the sphere).

The volume of the cavity was calculated by fitting images of the outline of the cavity with a piece-wise algebraic curve that comprises a sphere for the front section, an ellipse for the mid-section up to the widest part and then a rear parabolic section from the widest part to the tail. This is illustrated in fig. S4. The volume of the cavity, V_C can be evaluated analytically by integrating the 3-piece fitting function

$$V_C = \pi D_C^2 \left(\frac{L_E}{6} + \frac{2L_R}{15}\right) - 2\pi y_t^2 \frac{(L_E - L_T)}{3} + \frac{\pi(L_F - L_T)}{6}[3y_t^2 + (L_F - L_T)^2] \tag{S9}$$

Continuity of the 3-piece function and their tangents mean that

$$y_t = \sqrt{\frac{L_E^2 R_S^2 - R^4}{L_E^2 - R^2}}; \qquad L_T = \frac{L_E}{R}\sqrt{R^2 - y_t^2}$$

$$L_S = L_T - \sqrt{R_S^2 - y_t^2}\,; \qquad L_F = L_S + R_S; \qquad L = L_R + L_F$$

where the sphere diameter is $D_S = 2R_S$, cavity diameter is $D = 2R$, the ellipse semi-major axes are R and L_E and the length of the parabolic section is L_R.

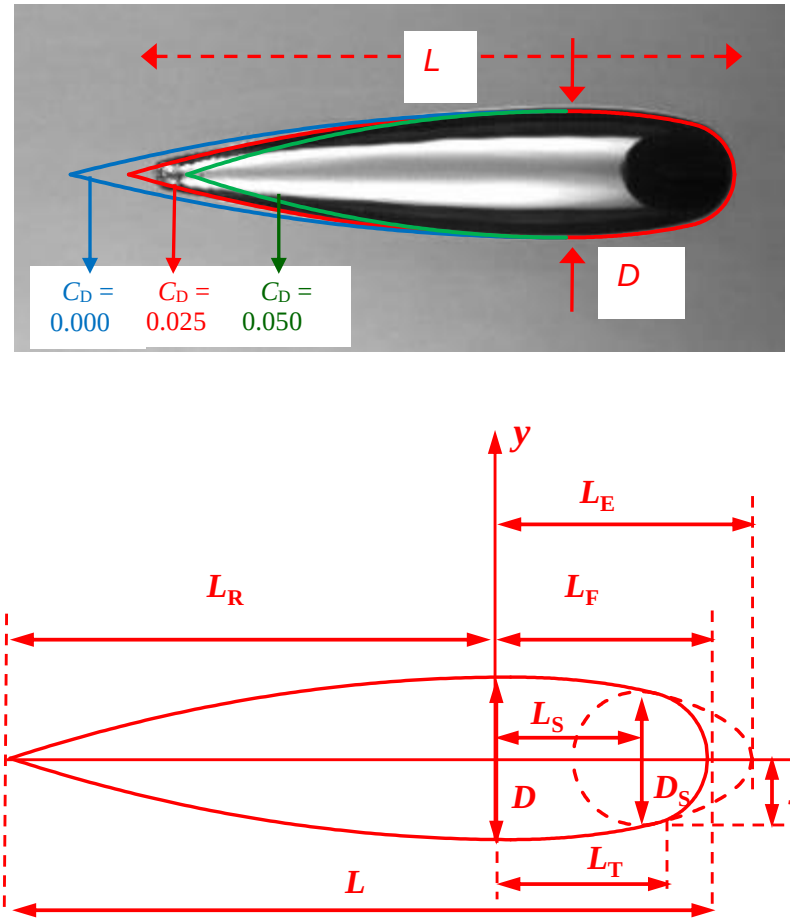

fig. S4. Three-piece fitting function for the sphere-in-cavity. Photograph of the sphere-in-cavity fitted by a spherical cap: $y = \pm\sqrt{R_S^2 - (x - L_F)^2}, L_T < x < L_S + R_S$; an elliptic mid-section: $y = \pm\left(\frac{D}{2L_E}\right)\sqrt{L_E^2 - x^2}, 0 < x < L_T$; and a parabolic tail: $y = \pm\left(\frac{D}{2}\right)[1 - (x/L_R)^2]$, $-L_R < x < 0$. The sensitivity of the drag coefficient to the fitting process is indicated for the sphere-in-cavity for a 20 mm diameter superhydrophobic steel sphere falling in room temperature water.

In our experiments the most sensitive parameter in the determination of the cavity drag coefficient is the cavity volume V_C. This is due to fact that the effective density of the sphere-in-cavity was only slightly higher than the density of the liquid, ρ ($1.0 < m_s/V_C < 1.1\rho$) and thus a small variation in the V_C gives a large variation in the C_D value. The examples in fig. S4 illustrate the sensitivity of the drag coefficient on the cavity shape fitting process. In the example given for a 20 mm steel superhydrophobic sphere falling in room temperature water the front part dimensions are fixed, and rear parabolic part contours correspond to drag coefficients: C_D = 0.025 (red line), C_D = 0.00 (outer blue line) and C_D = 0.050 (inner green line). For comparison the same shape and solid projectile drag coefficient was estimated to be about C_D = 0.200.

For the case of the projectile falling at terminal velocity, U the following modification of equation S1 is used to estimate the drag coefficient C_D

$$C_D = \frac{2g(m_P - \rho V_P)}{\rho\pi\, R_P^2\, U^2} \tag{S10}$$

where m_P is the mass of the projectile, and V_P is the projectile volume. The projectile volume V_P is precisely determined by the displaced water volume method, based on Archimedes' principle. The difference with the sphere-in-cavity experiments is that in the case of the projectile the mass of the projectile can be varied to increase m_P/V_P to about 2.0ρ, resulting in much smaller experimental uncertainties in determining C_D compared to the cavity case.

The free fall of the sphere-in-cavity formation and the solid projectile free fall were monitored with a high-speed video camera (Photron Fastcam SA-5) with a typical filming frame rate of 2000 fps. The location *vs* time and the corresponding instantaneous velocity was determined by image processing the videos with the camera software (Photron FASTCAM Viewer, PFV Ver.3262). In fig. S5 we show the variation of the velocity of sphere-in-cavity and the solid project when they are near the bottom of the tank, demonstrating that terminal velocity was achieved over a significant range of depth.

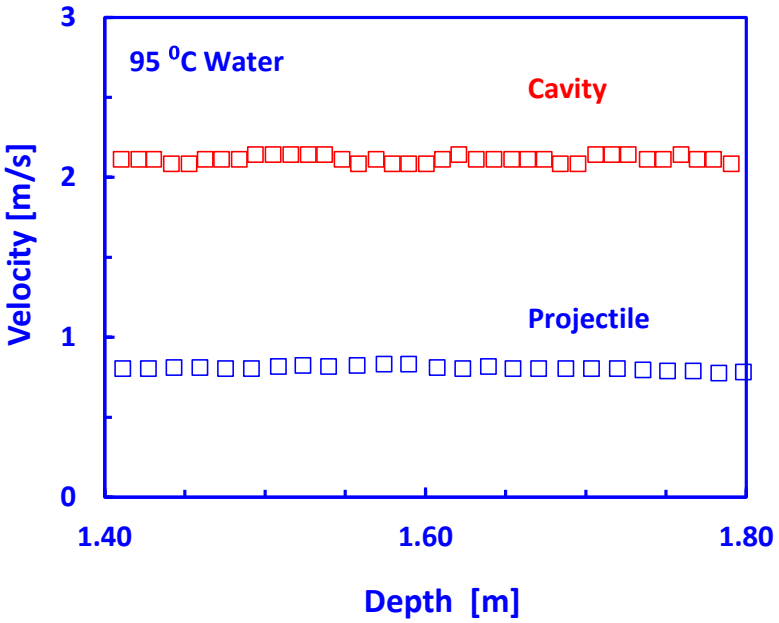

fig. S5. Velocity versus depth data. Experimental data for the free fall of sphere-in-cavity formed by the 20 mm steel Leidenfrost spheres, T_S = 400 ºC in 95 ºC water (open squares, red) and projectile of approximately same shape and buoyancy accounted weight (open squares, blue). Data shown are taken from movie S4.

In fig. S6 we compare the variation of the drag coefficient, C_D with the aspect ratio, (L/D) between solid projectiles and gas cavities. The key difference is that as L/D increases, the C_D for solid projectiles increases because of the increasing contribution of skin friction along the length of the projectile. In contrast, the C_D for solid projectiles decreases with increasing L/D because of the free slip boundary condition.

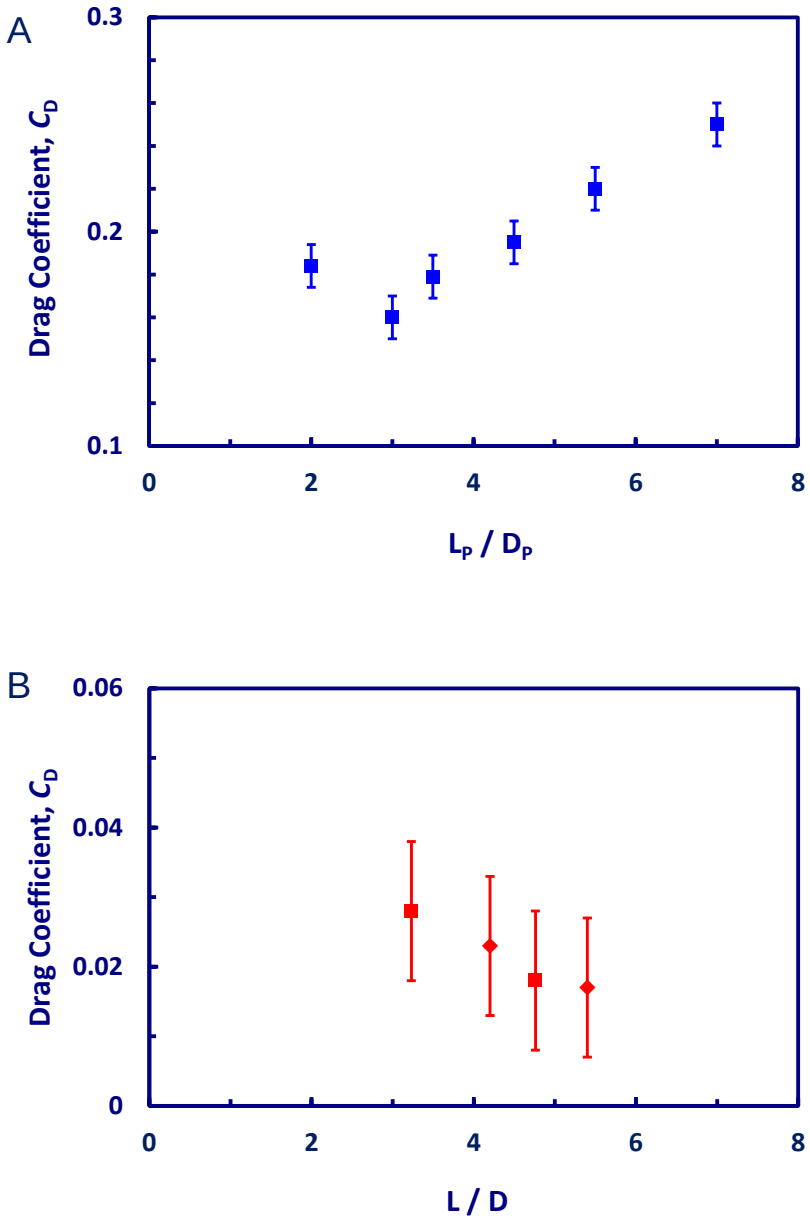

fig. S6. Dependence of the drag coefficient on the aspect ratio. (**A**) Variation of the drag coefficient, C_D of solid projectiles of D_P = 25 mm for a range of L_P/D_P ratios (blue squares). Each data point present the average values for projectiles Reynolds numbers variations between 2×10^4 and 10^5. (**B**) Variation of the drag coefficient, C_D of sphere-in-cavities for 20 mm steel or 20 mm tungsten carbide sphere in PP1 liquid (red squares), or in 95 ºC water (red rhombus).

table S1A. Physical parameters of the sphere-in-cavities in 95°C water. Leidenfrost steel or tungsten carbide (TC) spheres (T_S = 400 ºC) in 95 ºC water (ρ = 961 kg/m^3, μ = 0.3 × 10^{-3} Pa s).

Material	Sphere diameter D_S (mm)	Cavity diameter/length D (mm)/L (mm)	L/D	Release height h_r (cm)	Reynolds number Re	Sphere-in-cavity velocity U (m/s)	Drag coefficient C_D (± 0.01)
Steel	10	12.2/54	4.4	45	5.7×10^4	1.45	0.030
Steel	15	18.9/76	4.2	50	1.1×10^5	1.78	0.032
Steel	20	25.3/106	4.2	55	1.6×10^5	2.07	0.023
Steel	25	31.8/134	4.2	60	2.5×10^5	2.31	0.023
TC	10	14.4/82	5.6	45	1.0×10^5	2.22	0.012
TC	15	21.9/121	5.7	50	1.9×10^5	2.69	0.019
TC	20	28.4/156	5.5	60	9.1×10^5	3.09	0.018

table S1B. Physical parameters of the sphere-in-cavities in 21°C water. Superhydrophobic steel spheres in 21 ºC water (ρ = 998 kg/m^3, μ = 1.0 × 10^{-3} Pa s).

Material	D_S (mm)	D (mm)/L (mm)	L/D	h_r (cm)	Re	U (m/s)	C_D (± 0.01)
Steel	15	17.8/82	4.6	60	3.1×10^4	1.82	0.034
Steel	20	24.3/107	4.5	70	5.0×10^4	2.07	0.025
Steel	25	30.4/137	4.5	80	7.5×10^4	2.47	0.020

table S1C. Physical parameters of the sphere-in-cavities in PP1 liquid. Leidenfrost steel or tungsten carbide (TC) spheres (T_S = 230 ºC) in fluorocarbon liquid, PP1 (ρ = 1,716 kg/m^3, μ = 0.8 × 10^{-3} Pa s).

Material	D_S (mm)	D (mm)/L (mm)	L/D	h_r (cm)	Re	U (m/s)	C_D (± 0.01)
Steel	10	11.5/37	3.2	70	2.6 × 10^4	1.06	0.024
Steel	15	17.2/55	3.2	80	4.5 × 10^4	1.22	0.027
Steel	20	22.8/72	3.2	80	7.3 × 10^4	1.44	0.032
TC	10	12.8/59	4.59	70	4.3 × 10^4	1.58	0.020
TC	15	19.0/83	4.37	80	7.7 × 10^4	1.91	0.022
TC	20	25.1/117	4.68	90	1.2 × 10^5	2.22	0.018

movie S1. Free fall of sphere-in-cavity for 10-mm Leidenfrost steel sphere in PP1. Movie showing the steady velocity free fall of the sphere-in-cavity structure formed by the impact of a 10 mm Leidenfrost steel sphere, T_S = 230 ^{0}C in PP1 fluorocarbon liquid. The frame rate used was 3500 fps and the movie playback speed is 30 fps.

movie S2. Impact and cavity formation by 20-mm steel sphere in 21° and 95°C water. Combined movie tracking the formation of the sphere-in-cavity structure following the impact of a 20 mm Leidenfrost steel sphere, T_S = 400 ºC as it enters a 2 m tall tank containing water at 95 ºC (left movie) or of a superhydrophobic 20 mm steel sphere, T_S = 21 ºC at 21 ºC water (right movie). The frame rate used was 1000 fps and the movie playback speed is 30 fps.

movie S3. Close-up of sphere-in-cavity for 20-mm steel sphere in 21° and 95°C water. Higher magnification movie of the steady free fall of sphere-in-cavity structures in the case of a 20 mm Leidenfrost steel sphere, T_S = 400 ºC in 95 ºC water (left movie) or of a superhydrophobic 20 mm steel sphere, T_S = 21 ºC in 21 ºC water (right movie). The frame rate used was 2000 fps and the movie playback speed is 30 fps.

movie S4. Comparison of solid projectiles and sphere-in-cavity free fall. Combined movie showing the parallel fall of a solid projectile and a sphere-in-cavity of approximately the same shape and effective mass in the case of: 20 mm Leidenfrost steel sphere, T_S = 400 ºC in 95 ºC water (solid projectile first movie, sphere-in-cavity second movie from left) and a superhydrophobic 20 mm steel sphere, T_S = 21 ºC in 21 ºC water (projectile third movie, sphere-in cavity fourth movie from left). The frame rate used was 2000 fps and the movie playback speed is 30 fps.